In a recent study, we improved the SERS sensing performance of a tricyclazole (TCZ) sensor by employing a MnO_2/e-Ag nanocomposite as an active substrate, in comparison to the use of pure electrochemically synthesized silver nanoparticles (e-AgNPs). With a sulfur atom within the structure, TCZ could be linked to MnO_2 nanostructures via chemical bonds. Therefore, the presence of MnO_2 in the nanocomposite promoted more hot electrons from the e-AgNPs to be transferred to TCZ via a metal-to-semiconductor PICT pathway and then, a semiconductor-to-molecule IGCT pathway. This resulted in an EF of 1.38×10^6 when using MnO_2/e-Ag as the SERS substrate, which was 10 times higher than that when using pure e-AgNPs.[13] Similar enhancements were also described in the report of Zhou et al., who employed ZnO nanorods/AuNPs to detect dopamine in a SERS sensing system.[14] Therefore, taking advantage of the specific interaction between the desired analyte and the inorganic semiconductor, we designed a SERS active material to improve the Raman signal by promoting charge transfer via the IGCT pathway. However, there are numerous other compounds that are chemically inactive in the interaction with MnO_2, thus, it would not be convenient for them to experience the enhancement in CT arising on the nanocomposites. Thus, in this study, we aimed to continue modifying the nanomaterial to fill in the gap.

GO is a semiconductor material with abundant oxygen-containing groups, such as epoxide, carbonyl, and hydroxyl groups, which can be obtained by graphene modification. It can provide a large surface for the adsorption of various organic compounds.[15,16] Furthermore, GO can be an excellent supporter for the grafting of other materials, thus it has potential to be a component in hybrid materials.[17,18] There have been numerous studies into the construction of GO, semiconductor, and noble metals composite nanostructures as potential SERS substrates. For instance, Wang and co-authors utilized a novel $Ag/GO/TiO_2$ nanorod array as a SERS substrate for organic detection.[19] Zhang et al. successfully prepared a coating of GO on a TiO_2-AgNPs nanoarray for the rapid, accurate, and reliable detection of multiple organic pollutants, including crystal violet, rhodamine 6G, and malachite green. Hence, in this study, we chose GO nanosheets to modify our metal–semiconductor nanocomposite, MnO_2/e-Ag, and employed the as-prepared ternary structure as a SERS substrate for carbaryl (CBR), a pesticide that does not directly bind to MnO_2 via chemical bonds.

In this work, we employed MnO_2 nanosheets, GO nanosheets, and e-AgNPs, which were successfully fabricated as described in our previous studies,[13,20] to prepare ternary nanostructures via two simple steps: First, the MnO_2/GO structure was created using ultrasonication, followed by the grafting of e-AgNPs onto that structure by stirring. The detailed preparation is shown in Scheme 1. Subsequently, it was demonstrated that MnO_2/GO/e-Ag could improve the SERS signal of CBR, compared to the use of pure e-AgNPs, MnO_2/e-Ag, and GO/e-Ag substrates. In addition, by varying the GO content, the substrates were optimized. With the most optimal GO content of 0.1 wt%, MnO_2/GO/e-Ag could detect CBR at concentrations down to 1.11×10^{-8} M in standard solutions and 10^{-7} M in real samples of tap water and cucumbers.

2. Experimental

2.1. Materials and SERS substrates

Manganese dioxide (MnO_2) nanosheets, graphene oxide (GO) nanosheets, and e-Ag nanoparticles were synthesized as per our group's previous research.[13,20] Cabarryl (CBR), tricyclazole (TCZ), chloramphenicol (CAP), methylene blue (MB), and 4 nitrophenol (4-NP) were provided by Sigma-Aldrich. All chemicals were used directly without further purification. The utilized conical flasks and Teflon-lined hydrothermal autoclave were treated with aqua regia for 24 h before the experiments. In addition, the double-distilled water used in the whole process was purified through a Milli-Q® system (18.2 MΩ cm at 25 °C).

The aluminum (Al) substrate was prepared with dimensions of 1 cm × 1 cm × 0.2 cm with a surface-active area of diameter 0.2 cm. The substrate was cleaned properly. First, the substrates were soaked into a dilute hydrochloric acid solution to remove the oxide/hydroxide on the surface. Second, the substrate samples were washed with ethanol and double-distilled water by ultrasound for 15 min. Finally, the samples were dried naturally at room temperature.

2.2. Preparation of MnO_2/e-Ag nanocomposites

MnO_2/e-Ag nanocomposites were prepared as described in our previous report using two components: MnO_2 nanosheets and e-AgNPs with the most optimal ratio of 1 : 3.[13] Concerning the MnO_2 nanosheets, 30 mL of a mixed solution containing 0.67 M NaOH and 9.79 M H_2O_2 was divided into 20 aliquots and poured
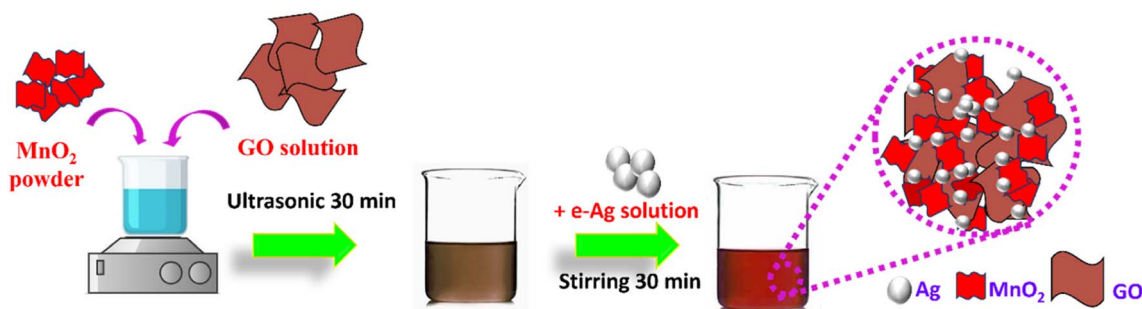
Scheme 1 Schematic illustration of the synthesis process of MnO_2/GO/e-Ag nanocomposites.

into 10 mL of 0.3 M $Mn(NO_3)_2$ solution, at a rate of an aliquot per minute under constant stirring. Then, the solution mixtures were stirred together for 30 min. The collected precipitate was washed 3 times with double-distilled water and then dried. The dried precipitate was dispersed in 2 M NaOH. This homogeneous solution was poured into a hydrothermal autoclave reactor and heated at a temperature T of 160 °C with a holding time of 16 h. The obtained product was centrifuged, washed three times with ethanol and distilled water, and then dried at 60 °C. On the other hand, e-AgNPs were prepared using an electrochemical method, which was fully described in another previous study of our group, resulting in the formation of citrate-coated e-AgNPs with an average diameter of 24 nm and ζ potential value of about −25 mV.[21] Subsequently, 50 mg of MnO_2 was dissolved in 50 mL of double-distilled water with the help of ultrasound to form a homogeneous suspension. Then, the MnO_2 solution was mixed with a certain volume of e-AgNP solution in a ratio of 1 : 3 and subjected to ultrasonic waves for 15 min. As a result, MnO_2/e-Ag was formed within the mixture. Full characterization of this nanocomposite was reported in our recent study.[22]

2.3. Preparation MnO_2/GO/e-Ag nanocomposites for SERS measurement

The MnO_2/GO/e-Ag nanocomposite was fabricated using the procedure described in Scheme 1. First, 50 mg of MnO_2 was completely dissolved in 50 mL double-distilled water under the aid of ultrasound treatment to form a homogeneous suspension. Then, the MnO_2 solution (1 mg mL^{-1}) was slowly added to a set of prepared mixtures containing different amounts of GO (0.05–0.5 wt%). GO was synthesized based on previous research.[20] The above-mixed solutions were ultrasonicated for 30 min. Next, a defined volume of e-AgNPs solution (1 mg mL^{-1}) was added to the above mixture solution and mixed well with magnetic stirring for 30 min. Thus, the MnO_2/GO/e-Ag nanocomposites were synthesized.

2.4. Characterization and SERS measurement

Scanning electron microscopy (SEM) was used to observe the morphology, and size of the prepared samples. The composition and chemical properties of MnO_2/GO/e-Ag were investigated by Raman spectroscopy (Horiba Macro-RAMt) with 785 nm laser excitation.

SERS active materials (i.e., AgNPs, MnO_2/e-Ag, and MnO_2/GO/e-Ag) were loaded onto the surface-active area of the Al substrates via evaporation. In detail, for each measuring substrate, 5 μL SERS active material solution was drop-cast directly on to the surface-active area of the Al substrate. Then it was dried at 50 °C before being used for SERS measurement.[21] CBR solutions with different concentrations (10^{-3}–10^{-8} M), TCZ (10^{-5} M), MB (10^{-5} M) CAP (10^{-3} M), and 4-NP (10^{-3} M) were prepared in distilled water before being dropped directly onto the prepared substrates. After that, they were dried naturally at room temperature and taken to perform the SERS measurements. The SERS spectra were monitored by a MacroRaman™ Raman spectrometer (Horiba). Raman measurements were acquired by means of a 100×

objective with a numerical aperture of 0.90. The laser power was set to 45 mW at a 45° contact angle, with a focal length of 115 nm. An exposure time of 10 s was used with three accumulations. At every point of the SERS measurement, the experiment was repeated three times.

Cucumbers were purchased from a local supermarket and washed thoroughly using deionized water. Then the cucumbers were minced and mashed. Next, 25 g of the obtained cucumber was mixed with 30 mL of double-distilled water by a vortex mixer. The mixture was filtered with Whatman filter paper. Finally, the cucumber extract was collected. CBR standard solution at different concentrations was added into the cucumber extract samples. Subsequently, 5 μL spiked sample was drop-cast directly on to the prepared SERS substrates for SERS measurements under ambient room conditions.

To test the CBR detection in the tap-water sample, the experiments were conducted as follows. Different concentrations of CBR in the linear range (10^{-4}–10^{-7} M) were prepared directly utilizing tap water, which was taken from the local area. Next, 5 μL CBR solution was drop-cast directly on to the prepared SERS substrates for the SERS measurements under ambient room conditions.

3. Results and discussion

3.1. Importance of the chemical bonds in the SERS effect on MnO_2 nanosheets

To confirm the importance of chemical bonds in the SERS effect on the MnO_2/e-Ag substrate, we evaluated the SERS enhancement of two groups of organic compounds. Group 1 consisted of chemicals that were reported to be degraded by MnO_2, thus, there would be chemical interactions between the semiconductor and the organic compounds, such as tricyclazole (TCZ) and methylene blue (MB). The chemicals in Group 2, in contrast, have not been reported to be degraded in the presence of MnO_2. Moreover, they possessed no specific functional group to bind directly to MnO_2 nanosheets via chemical bonds. The molecular structures of the chemicals in Group 1 and Group 2 are shown in Table S1.†

Concerning Group 1, the interaction between TCZ and MnO_2 via the S atom of TCZ was fully described in our previous study.[13] This chemical bond allows hot electrons to be transferred from MnO_2 to TCZ via an interfacial ground-state charge-transfer (IGCT) pathway. Thus, using MnO_2/e-Ag nanocomposite as a SERS substrate, MnO_2 would act as a bridge for CT from the laser-excited e-AgNPs to TCZ. As a result, more hot electrons can be transferred from the plasmonic nanomaterial to the analyte, leading to enhancements in the SERS signal of TCZ on MnO_2/Ag, compared to the use of pure e-AgNPs alone. In detail, at the concentration of TCZ (10^{-3} M), the SERS intensity of TCZ on MnO_2/e-Ag, measured by the peak of 431 cm^{-1}, was estimated to be 6.66 times higher than that on AgNPs. This result was presented in our previous study.[13] Similar to TCZ, MB was reported to be degraded by MnO_2. In a 2021 study, Yan et al. employed XPS characterization to confirm that the N atom within the benzene ring of MB could be directly linked to the MnO_2 surface.[23] Thus, it was expected that MnO_2/e-Ag could
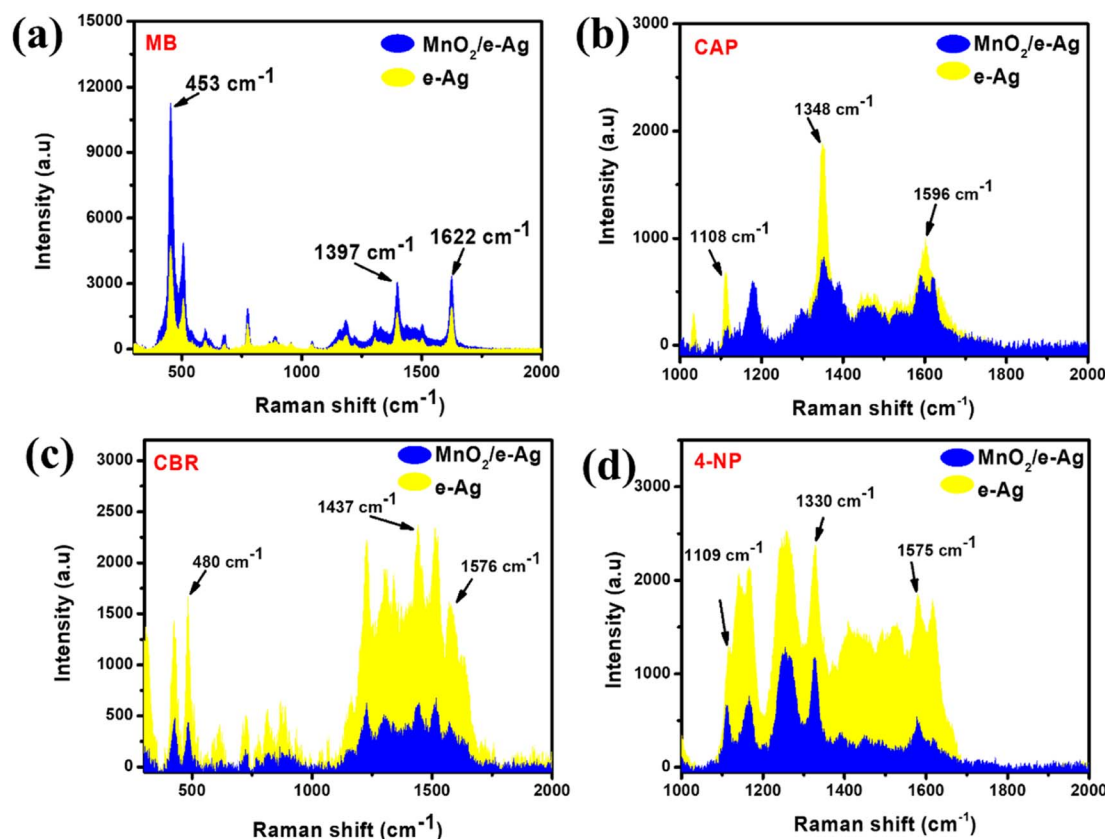
Fig. 1 SERS intensities of (a) MB (10^{-5} M), (b) CAP (10^{-3} M), (c) CBR (10^{-3} M), and (d) 4-NP (10^{-3} M) at the characteristic peaks on e-Ag, and MnO$_2$/e-Ag nanocomposites.

enhance the Raman signal of MB better than pure e-AgNPs. This hypothesis was confirmed by the SERS measurements of MB (10^{-5} M) on MnO$_2$/e-Ag and pure e-AgNPs, as shown in Fig. 1a. On the MnO$_2$/e-Ag substrate, the SERS intensity of MB was obviously higher than that on pure e-AgNPs. For the characteristic peaks of 453, 1393, and 1622 cm^{-1}, the SERS intensities of MB on MnO$_2$/Ag were 2.83, 1.61, and 1.69 times higher than those on pure AgNPs. In contrast, the organic compounds in Group 2 were not reported to be degraded or linked to MnO$_2$ *via* chemical bonds. The SERS spectra of chloramphenicol-CAP (10^{-3} M), carbaryl-CBR (10^{-3} M), and 4 nitrophenol-4-NP (10^{-3} M) on MnO$_2$/Ag were compared to those on pure AgNPs, as shown in Fig. 3b–d, respectively. It was clear that on the MnO$_2$/Ag substrate, the Raman signals of the organic compounds in Group 2 were less enhanced, compared to those on pure AgNPs, at their characteristic peaks. The assignments for the characteristic peaks of MB, CAP, CBR, and NP are listed in Table S1.† This result confirmed the importance of the chemical bonds between the substrate and the analyte in SERS enhancement. Furthermore, it raised a question of how to improve the sensing performance of SERS sensors for analytes that do not bind directly to the active substrates *via* chemical bonds. GO, with its excellent adsorbing ability, would be a solution for further material modification to overcome this obstacle.

3.2. Characterization of MnO$_2$/GO/e-Ag nanocomposite

A set of MnO$_2$/GO/e-Ag composites was prepared with different GO contents ranging from 0.05–0.5 wt%. Meanwhile, the Ag content of 75% was proven to be effective for the SERS phenomenon arising in our previous study,[13] thus, this was fixed as the Ag content within every composite in this study. The contents of the components were calculated based on their weight added during preparation. Fig. 2a shows the Raman spectrum of MnO$_2$/GO/e-Ag, indicating the presence of all three components. Two characteristic peaks of GO could be observed at ~1313 cm^{-1} (D band) and ~1605 cm^{-1} (G band), representing the breathing modes of the rings (K-point phonons) with the A$_{1g}$ symmetry and the in-plane bond-stretching E$_{2g}$ mode of C sp^2 atoms, respectively.[24] In addition, the spectrum exhibited two bands at 585 and 645 cm^{-1}, which were assigned to the symmetric Mn–O vibrations and are characteristic of α-MnO$_2$ with a (2 × 2) tunnel.[25] Besides, the band at 240 cm^{-1} was associated with the stretching vibrations of Ag–O bonds.[26] Additionally, the presence of MnO$_2$, Ag, and GO in the nanocomposite was also confirmed by the XRD pattern, as shown in Fig. 2b. The XRD result revealed the tetragonal crystal system of α-MnO$_2$ with intense and sharp peaks for the (110), (200), (310), (400), (301), (600), and (521) crystal phase corresponding to JCPDS card no. 44-0141. The main diffraction peaks of Ag for the (111), (200), and (220) planes also existed in the XRD pattern
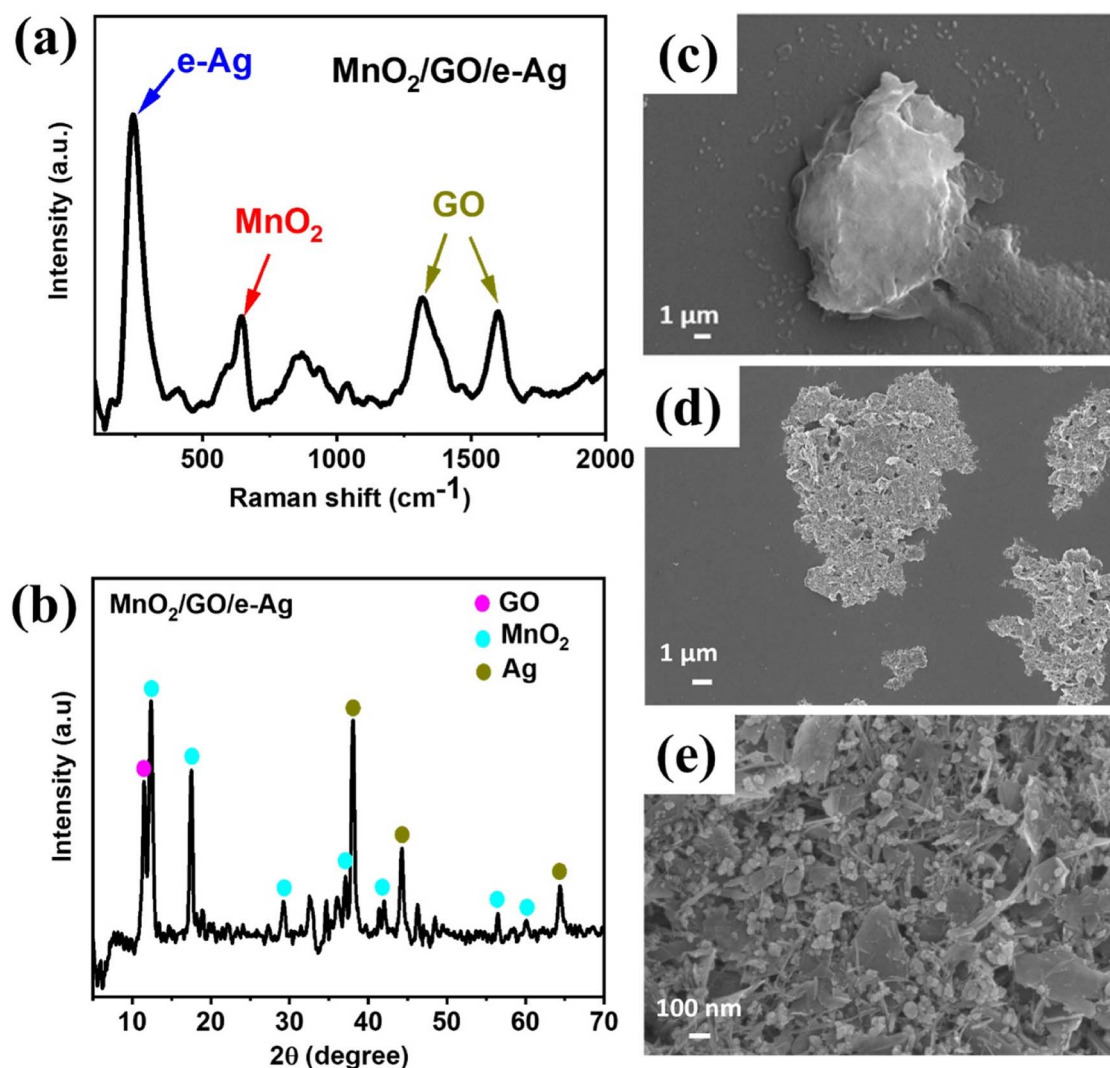
Fig. 2 Raman spectrum of (a) $MnO_2/GO/e$-Ag; XRD pattern of (b) $MnO_2/GO/e$-Ag (with 0.1 wt% of GO); SEM images of (c) GO and (d and e) $MnO_2/GO/e$-Ag (with 0.1 wt% of GO) at different magnitudes.

(JCPDS no. 01-087-0719). The characteristic peak of GO was obtained at $2\theta = 11.5°$, revealing the reflection plane (001).[27] Moreover, the formation of the nanocomposite was also confirmed by the SEM images. Due to the exceptional brightness of e-AgNPs compared to MnO_2 and GO nanosheets under the electron microscope and low content of GO in the nanocomposite (0.1 wt%), unfortunately we could not observe the presence of GO in Fig. 2d and e. However, Fig. 2d shows that MnO_2 nanosheets and e-AgNPs had gathered together to create micro-sized structures, corresponding to the structure displayed in Fig. 2c, which was formed by layers of GO nanosheets. Therefore, MnO_2 could have covered GO sheets during the preparation of MnO_2/GO *via* ultrasonication, followed by the grafting of e-AgNPs onto this material. The assembly of MnO_2 on GO sheets could be observed more clearly in Fig. S6a and b.† Without the bright e-AgNPs, the MnO_2 nanostructures can be detected as small flakes on the large GO surface. With a higher content of GO, namely 2.0 wt% in $MnO_2/GO/e$-Ag

nanocomposites, which would be referred to as 0.5 wt% in $MnO_2/GO/e$-Ag nanocomposites, the surface of the GO sheet could be better observed in Fig. S6b.† In contrast, when the GO content was five-times lower, MnO_2 flakes covered it more properly (Fig. S6a†), forming a nest for harboring the e-AgNPs (Fig. 2e). Thus, the GO content influenced the structure of MnO_2/GO. Its effects on $MnO_2/GO/e$-Ag then its SERS performance will be further discussed in the following sections.

3.3. Effects of GO content on SERS analytical performance of the $MnO_2/GO/e$-Ag nanocomposites-based sensing platform

To investigate the effect of GO and its content on the SERS performance of $MnO_2/GO/e$-Ag nanocomposites-based SERS sensors, we measured and compared the SERS signals of CBR (10^{-3} M) on pure e-AgNPs and four types of $MnO_2/GO/e$-Ag nanocomposites with different contents of GO (0.01, 0.1, 0.3, and 0.5 wt%) (Fig. 3a). On all the substrates, the SERS spectra exhibited characteristic peaks of CBR at 480, 723, and
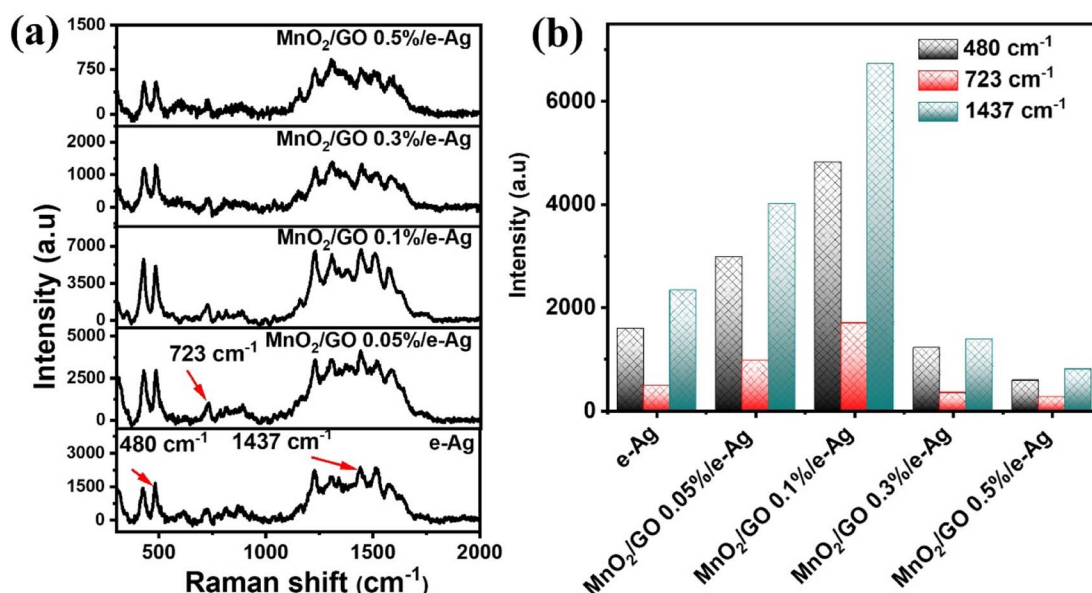
Fig. 3 (a) SERS spectra of CBR (10^{-3} M) on e-AgNPs, and MnO$_2$/GO/e-Ag nanocomposites with different GO contents. (b) SERS intensities of CBR (10^{-3} M) at 480, 723, and 1440 cm^{-1} on e-AgNPs, and MnO$_2$/GO/e-Ag nanocomposites with different GO contents.

1440 cm^{-1}. However, they showed significant differences in SERS intensity, revealing the levels of their sensing performance. Comparisons of the SERS intensities at 480, 723, and 1440 cm^{-1} are presented in Fig. 3b. With the addition of only 0.05 wt% of GO, the SERS intensity of CBR obviously increased, compared to the use of pure e-AgNPs. It is worth remembering that without GO, the SERS intensities at 480, 723, and 1440 cm^{-1} of CBR on MnO$_2$/e-Ag were 3.38, 3.02, and 2.83 times lower those on pure e-AgNPs, respectively (Fig. 1c). Moreover, they increased with the increase in GO content from 0.05 to 0.1 wt%. However, when the GO content reached 0.3 wt%, the SERS intensity of CBR dropped, and it was even lower than when using pure e-AgNPs. This downward trend continued when the GO content was raised to 0.5 wt%. Therefore, GO and its content showed noticeable effects on the SERS enhancement of CBR on these Ag-based substrates. In addition, using a GO content of 0.1 wt% in MnO$_2$/GO/e-Ag nanocomposite as a SERS substrate for CBR detection resulted in an enhancement factor (EF) of 1.10×10^6, which was 5.88 times higher than that when using e-AgNPs (EF = 1.87×10^5). The EF values were calculated as described in the ESI.† GO has been reported to be an excellent adsorbent for organic compounds. Many studies have also claimed that GO exhibited favorable adsorption sites for aromatic compounds,[28–30] thanks to π–π and hydrophobic interactions. Although these interactions are not as strong as chemical bonds, which highly promote charge transfer, this adsorbent could allow more analytes, especially aromatic ones, to be adsorbed onto the substrate. As a result, more analytes could experience a SERS effect originating from e-AgNPs. With a naphthalene ring, which is a fusion of two aromatic rings, in the structure, CBR would have been well-adsorbed onto MnO$_2$/GO/e-Ag thanks to the presence of GO nanosheets. However, it was not only GO that was responsible for the improvement of

the SERS signal of CBR on MnO$_2$/GO/e-Ag in comparison to the use of pure e-AgNPs. Fig. S1† shows that also with a GO content of 0.1 wt%, the use of the GO/Ag nanocomposite did not result in better SERS enhancement than when using pure e-AgNPs alone. This emphasizes the role of the integration between MnO$_2$ and GO within MnO$_2$/GO/e-Ag for improving the SERS performance of the sensing platform. As mentioned in the previous section, this GO content led to the formation of nest-like MnO$_2$/GO structures (Fig. S6a†) for the anchoring of e-AgNPs. Besides, this porous structure of the composite could provide a larger surface area for the adsorption of CBR. When increasing the GO content to three- and five-time higher (i.e., 0.3 wt% and 0.5 wt%), the GO nanosheets could have veiled MnO$_2$ nanostructures during MnO$_2$/GO preparation, preventing them forming such a porous structure, and preventing CBR being well adsorbed onto the active substrate, leading to a remarkable decrease in SERS intensity, as shown in Fig. 3b. Fig. S6b† shows that with a high GO content, MnO$_2$/GO did not exhibit the nest-like morphology. Instead, a large surface of GO was revealed. Although in this sample, the GO content was five-times higher than that in Fig. S6a,† it was still extremely smaller than the MnO$_2$ content. Therefore, there was no such significant difference in MnO$_2$ content within those two structures, and the slightly lower content of MnO$_2$ should not be responsible for the fact that the MnO$_2$ nanosheets did not properly cover the GO surface. Instead, with a closer look at the GO surface in Fig. S6b,† we could observe flake-like structures covered by the GO sheet, confirming our hypothesis. Therefore, the GO content of 0.1 wt% was the most optimal for MnO$_2$/GO/e-Ag as an active SERS substrate for CBR detection. On this substrate, the SERS signals of other compounds in Group 2, including CAP and 4-NP, were also enhanced, as shown in Fig. S2.† Hence MnO$_2$/GO/e-Ag could be employed as the SERS

© 2023 The Author(s). Published by the Royal Society of Chemistry

substrate to sense other organic molecules. However, in this study, we selected MnO_2/GO/e-Ag nanocomposite with the most optimal GO content of 0.1 wt% to develop SERS sensors for CBR.

To confirm that the MnO_2/GO/e-Ag nanostructure with a GO content could improve the adsorption capacity of CBR, we performed an electrochemical model. Related to the electroactive surface area (EASA) of the modified electrodes using e-AgNPs, MnO_2/e-Ag, and MnO_2/GO/e-Ag (with 0.1 wt% of GO), cyclic voltammetric (CV) measurements were carried out in 0.1 M KCl containing 5 mM $[Fe(CN)_6]^{3-/4}$ and at various scan rates ranging from 10–60 mV s^{-1}, as shown in Fig. 4. Changes in the response current intensity and the reversible redox peak potential could be detected while using every modified electrode. Corresponding linear plots were recorded between the peak current (I_p, μA) and the sqrt. of the scan rate ($v^{1/2}$). Therefore, the redox reactions on the electrode surface exhibited a diffusion process.

The EASA value was calculated based on the Randles–Sevick equation:[31–33]

$$I_p = 2.69 \times 10^5 \times n^{3/2}D^{1/2}ACv^{1/2} \qquad (1)$$

where I_p is the peak current intensity, n is the number of electrons transferred ($n = 1$), D is the diffusion coefficient of $[Fe(CN)_6]^{3-/4-}$ ($D = 6.5 \times 10^{-6}$ cm s^{-1}), A is the EASA value, v is the scan rate, and C refers to the bulk concentration of the redox probe. The value of EASA was estimated to be about 0.137 cm^2 for Ag/SPE, 0.212 cm^2 for MnO_2/e-Ag_SPE, and 0.223 cm^2 for MnO_2/GO/e-Ag_SPE. Thus, the MnO_2/GO/e-Ag electrode had the largest active surface area.

CV measurements in pH 7 PBS buffer containing 50 μM CBR were carried out in the scan rate range from 20 to 70 mV s^{-1} to investigate the response kinetics of CBR on the modified electrodes. Fig. 5 presents the impact of varying the scan rate (20–70 mV s^{-1}) on the electrochemical behaviors of CBR. The above results showed that as the scanning speed increased, all electrodes' anode/cathode maximum current gradually increased. Images 2a', b', and c' showed a highly linear relationship between I_{pa} and v, with the linear regression equations as follows:

$$I_p (\mu A) = 0.132\, v\, (mV\ s^{-1}) + 0.494\ (R^2 = 0.99)\ \text{for e-Ag\_SPE}$$

$$I_p (\mu A) = 0.162\, v\, (mV\ s^{-1}) + 0.79\ (R^2 = 0.99)\ \text{for } MnO_2\text{/e-Ag\_SPE}$$

$$I_p (\mu A) = 0.23\, v\, (mV\ s^{-1}) + 1.07\ (R^2 = 0.99)\ \text{for } MnO_2\text{/GO/e-Ag\_SPE}$$

Based on these linear relationships, the adsorption capacity (Γ) of CBR on the modified electrode surfaces was also determined through the equation:[34] $I_p = n^2F^2A\Gamma v/4RT$. According to that, the Γ values of CBR were estimated to be around 19.4×10^{-12}, 20×10^{-12}, and 25.7×10^{-12} mol cm^{-2} for e-Ag_SPE, MnO_2/e-Ag_SPE, and MnO_2/GO/e-Ag_SPE, respectively. Clearly, the MnO_2/GO/e-Ag modified electrode possessed the largest Γ value of CBR, followed by MnO_2/e-Ag and then e-Ag. The increase in electrode active surface area would be related to the increase in adsorption capacity of the analyte. The improvement in adsorption capacity of CBR on MnO_2/GO/e-Ag indicated that the nanocomposite could adsorb the largest number of CBR molecules compared to the other materials, allowing them to experience the SERS effect by a chemical enhancement mechanism, resulting in the best enhanced Raman signal. This result confirms the importance of GO in the nanocomposite as a SERS substrate for the effective detection of CBR.
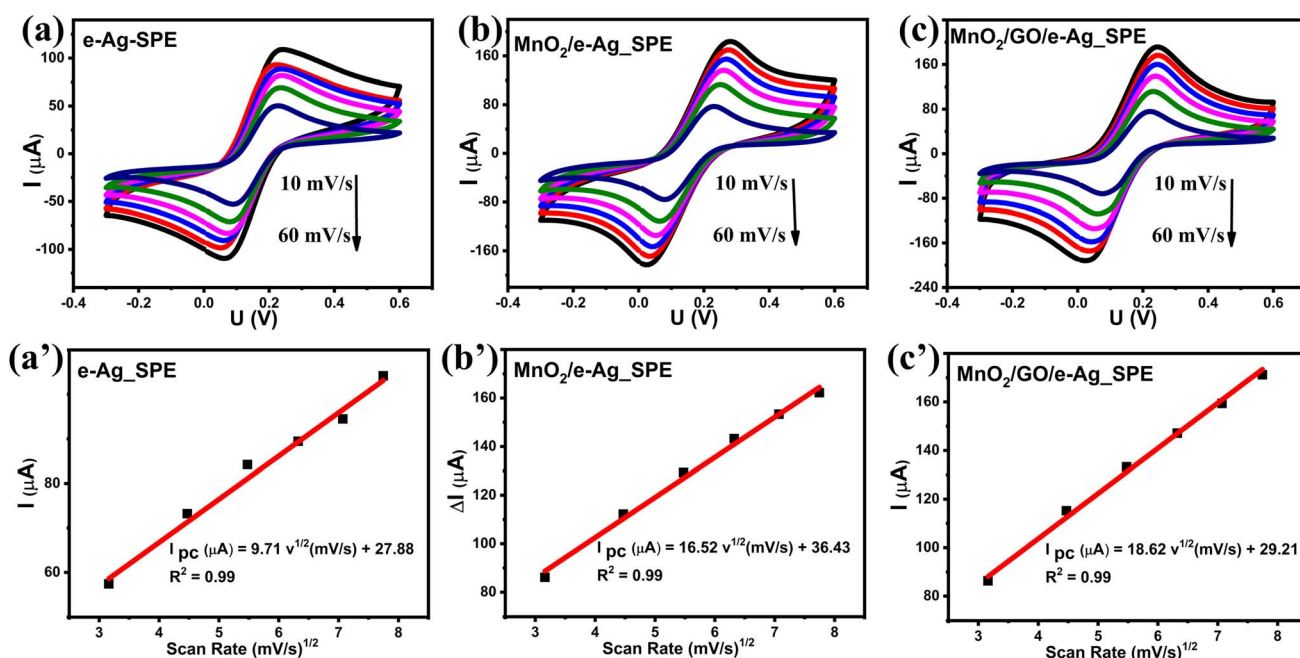

Fig. 4   (a–c): CV curves of the proposed electrodes at various scan rates (10–60 mV s^{-1}) in 0.1 M KCl containing 5 mM $[Fe(CN)_6]^{3-/4-}$; and (a'–c'): corresponding linear plots of the reduction in peak current against the square root (sqrt.) of the scan rate.
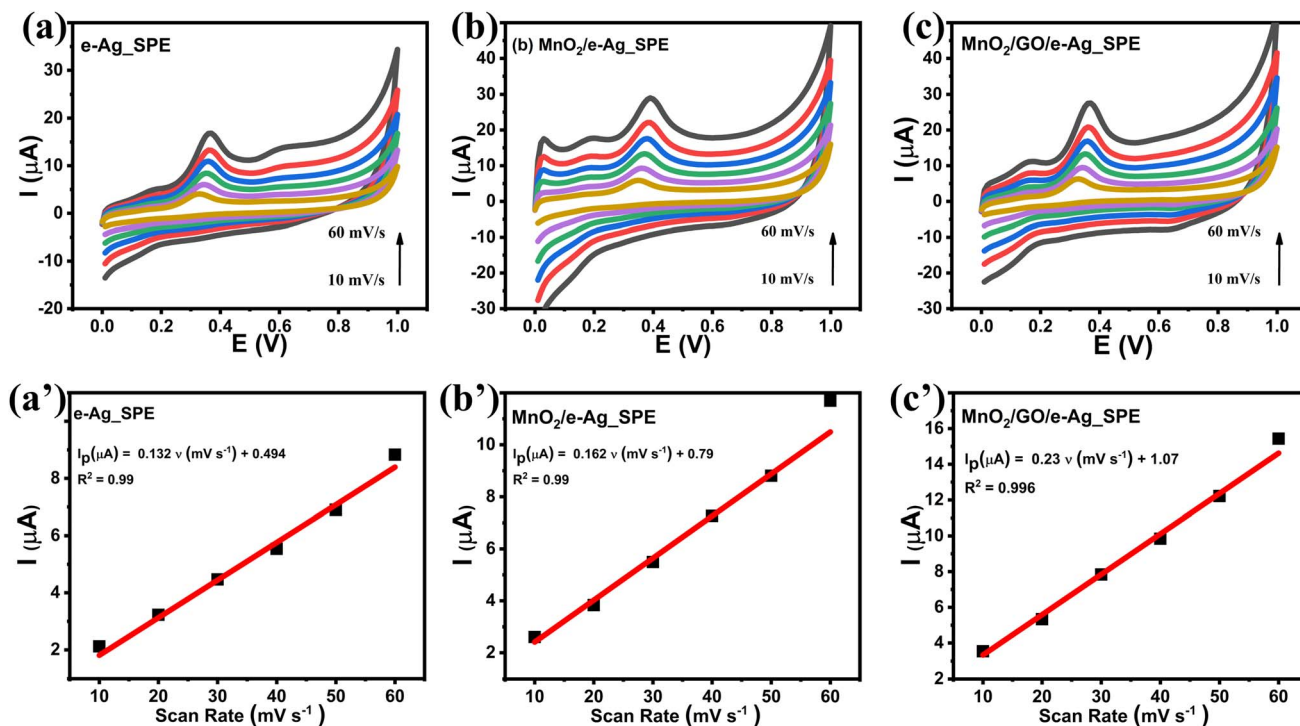
Fig. 5 (a–c): CVs responses of 50 μM CBR at the modified electrodes in 0.1 M PBS buffer at different scan rates, and (a'–c'): plots of the peak current (*I*) versus scan rate (*v*).

3.4. SERS performance of MnO₂/GO/e-Ag nanocomposites-based carbary sensors

Fig. 6a displays the SERS spectra of CBR at various concentrations (10^{-3}–10^{-8} M) on MnO₂/GO/e-Ag (with 0.1 wt% of GO). As CBR is a naphthalene-derivatized carbamate, the characteristic peaks of CBR were dominated by ones associated with naphthalene and the carbamate vibrational mode. The band at 453 cm^{-1} was assigned to the low-frequency C–C bending modes. The band at 723 cm^{-1} was associated with NCOC bending with some ring breathing character. The band at 1374 cm^{-1} represented the symmetric ring vibration modes. The band at 1437 cm^{-1} was assigned to the C–H wagging mode, while that at 1576 cm^{-1} was related to the C=C stretching mode in the naphthalene ring.[35–38] The SERS spectra of CBR on MnO₂/GO/e-Ag substrate were consistent with the Raman spectrum of CBR (Fig. S3†).

With the decrease in the CBR concentration from 10^{-3} M to 10^{-8} M, the typical peak intensity of CBR pesticide demonstrated a sharp decline. When the concentration was the lowest at 10^{-7} M, the characteristic absorption bands of CBR at 480 cm^{-1} could be still distinctly observed, showing that the MnO₂/GO/e-Ag material exhibited the effective sensitivity of the sensor to CBR pesticide detection, which was similar to some SERS sensors for CBR (Table 1). Fig. 6b shows a plot of the logarithmic SERS intensity at 480 cm^{-1} against the logarithmic concentration of CBR with a linear relationship in the region from 10^{-4}–10^{-7} M ($R^2 = 0.93$). The detection limit of the sensor was 1.11×10^{-8} M (∼0.003 ppm), which was much lower than the maximum residue limit (MRL) for farm

products (10 ppm).[39] The quantification range from 10^{-4}–10^{-7} M (∼0.03 ppm to ∼30 ppm) of the sensor also covered MRLs for food, such as cucumber (3 ppm), corn (1 ppm), and milk (0.05 ppm), established by Food and Agriculture Organization of the United Nations (FAO). Thus, it has the potential for food safety monitoring. Moreover, this MnO₂/GO/e-Ag substrate also presented relatively good uniformity in the detection of CBR on 30 different points on a MnO₂/GO/e-Ag substrate containing CBR (10^{-5} M) (Fig. 6c). The RSD was calculated to be 14.03%. In addition, the reproducibility of the substrate was determined by measuring the SERS signal of CBR (10^{-5} M) on five MnO₂/GO/e-Ag substrates, which were prepared similarly to each other, as shown in Fig. 6d. The RSD was determined to be 10.65%. The LOD and RSD values were calculated as described in the ESI.†

3.5. Practicability of the MnO₂/GO/e-Ag nanocomposites-based CBR sensors with real samples of tap water and cucumber

In order to evaluate the efficiency of the SERS sensor and their applications in real samples, CBR at four concentrations from 10^{-4}–10^{-7} M were detected in tap water and cucumber extract samples. Fig. 7a and c display the SERS spectra of CBR in tap water and cucumber extract, respectively. They all exhibited characteristic peaks of CBR, which were similar to the standard solutions (Fig. 6a). However, the spectra of CBR in the cucumber extract sample showed several minor shifts and a few new peaks, which might be related to the interaction of the available components in the real sample, such as
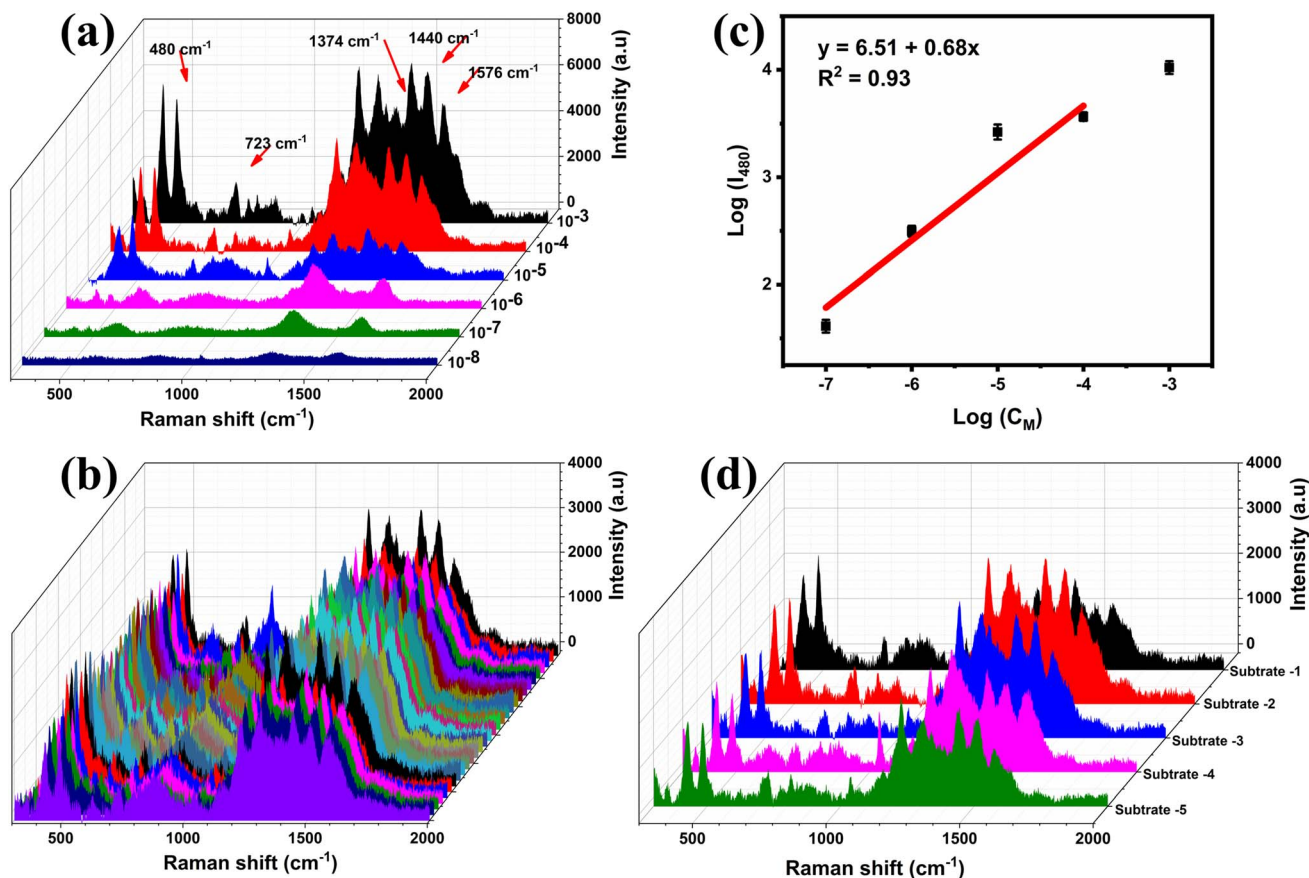
Fig. 6 (a) SERS spectra of CBR (10^{-3}–10^{-8} M) on MnO$_2$/GO/e-Ag. (b) Plot of the log of SERS intensity at 480 cm^{-1} against CBR concentration. (c) Uniformity and (d) reproducibility of SERS sensors for CBR (10^{-5} M) using the MnO$_2$/GO/e-Ag substrate (with 0.1 wt% of GO).

Table 1 Comparison with other CBR sensors

Material	LOD	Linear range	Ref.
Ag nanoparticles-coated Si nanowire-SiNW	1.00×10^{-7} M	10^{-2}–10^{-7} M	39
Poly(ethyleneterephthalate) PET/ITO/Ag	$\sim 4.00 \times 10^{-7}$ M	—	40
Gold nanorod arrays	$\sim 2.5 \times 10^{-6}$ M	0–1.5×10^{-4} M	41
Silver nanoparticles on cotton swabs	5×10^{-7} M	5×10^{-4}–5×10^{-7} M	42
MnO$_2$/GO/e-Ag	1.11×10^{-8} M	10^{-3}–10^{-7} M	This work

carbohydrate, pectin, and minerals. In tap water, inorganic ions could also be absorbed onto the SERS substrate. These constituents could inhibit the connection between the target analytes and the nanoparticles surface, thus reducing the enhancement signals of the SERS substrate.[43] However, the ternary material could detect CBR in real samples at concentration down to 10^{-7} M (~ 0.03 ppm) (Fig. 7b and d), which is lower than the maximum residue limit (MRL) for cucumbers and other melons established by the FAO (3 ppm). The recovery rates ranged from 84–107% with RSDs of 9.70–13.46% in tap water and from 87–111% with RSDs of 7.42–13.57% in cucumber extract (Table S2†), indicating the high accuracy of the sensing system when employed for the

detection of CBR in real samples. However, real samples are usually complicated with interferences from other chemical compounds in addition to the targeted analyte. For example, a vegetable sample may contain more than one pesticide. Therefore, in this study, we designed an experiment to determine the presence of CBR in cucumber samples containing two other pesticides: 4-nitrophenol and glyphosate. As previously mentioned, CBR did not form any specific bonds with MnO$_2$/GO/e-Ag; therefore, the sensing platform did not exhibit high selectivity as the SERS spectra showed characteristic peaks of all those pesticides with much noise (Fig. S4†). However, it is worth stressing that in the interferences of the other two, the characteristic peak at 480 cm^{-1} of
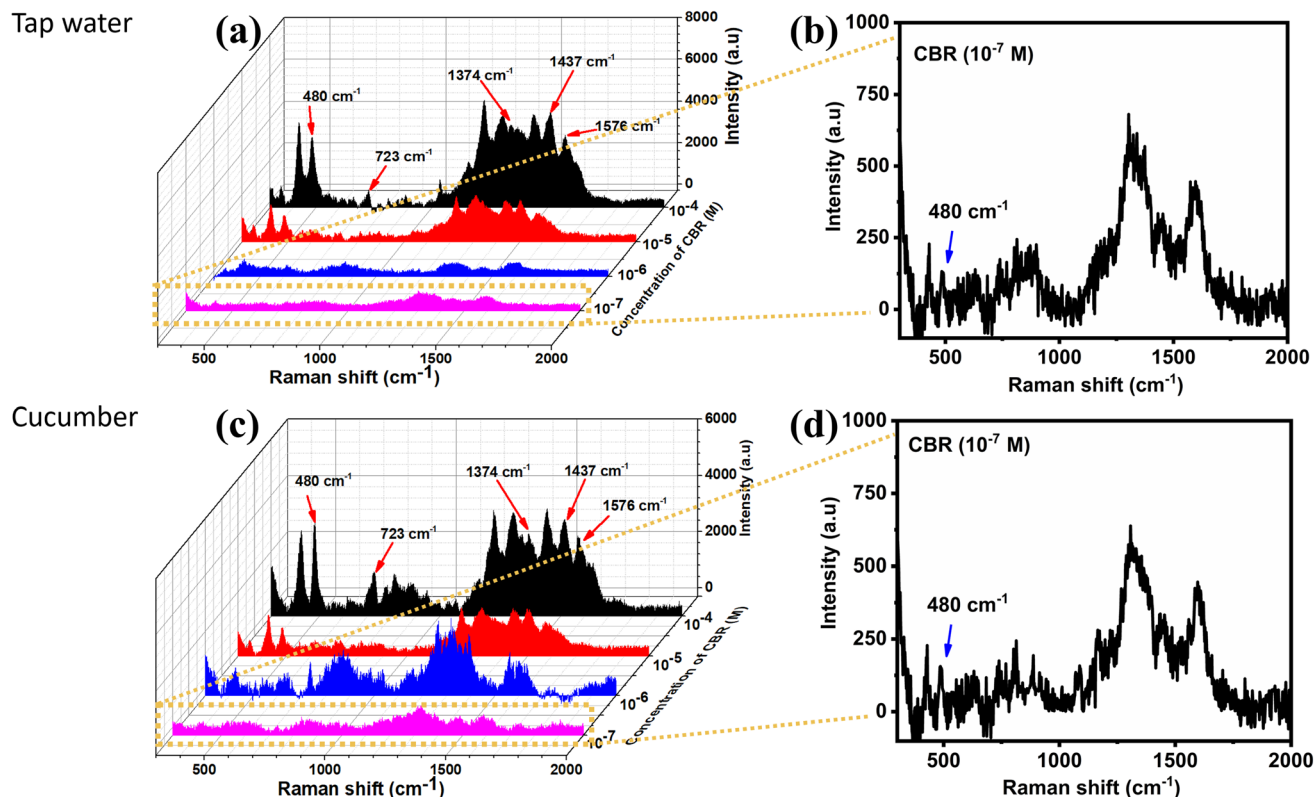
Fig. 7 SERS spectra of TCZ (10^{-4}–10^{-7} M) in real samples of (a) tap water and (c) cucumber on the MnO_2/GO/e-Ag (with 0.1 wt% of GO) SERS substrate; SERS spectra of CBR (10^{-7} M) on MnO_2/GO/e-Ag (with 0.1 wt% of GO) in (b) tap water, and (d) cucumber samples.

CBR could still be detected at concentrations down to 10^{-6} M. Based on the intensity of the peak, the CBR concentration could be calculated with recoveries of 94–110% and RSDs of 11.54–14.52% (Table S3†).

4. Conclusions

In this work, we performed a modification of the MnO_2/e-Ag substrate reported in our recent research due to its limited ability to form links between the substrate and organic molecules. In summary, we successfully fabricated a sensitive and reliable MnO_2/GO/e-Ag nanocomposite SERS substrate for the detection of carbaryl pesticide through some simple mechanical methods, including ultrasound and stirring. The influence of GO on the SERS sensing performance of the MnO_2/e-Ag nanocomposite was systematically investigated. The results displayed that the synergistic effects of MnO_2 and GO nanosheets endowed the sensing substrate with improved sensitivity, repeatability, uniformity, and stability. With the GO content of 0.1 wt%, the SERS sensor exhibited low detection limits for CBR (1.11×10^{-8} M in standard solutions and 10^{-7} M in real samples of tap water and cucumber extract). Moreover, the composite nanomaterial could also enhance the SERS signals of other organic compounds that do not bind directly to MnO_2, such as CAP and 4-NP. Hence, this upgraded MnO_2/GO/e-Ag nanocomposite will be an ideal SERS substrate with broad applications for the rapid detection of organic residues.

Author contributions

D. T. N. Nga: conceptualization, validation, investigation, Q. D. Mai: validation, investigation; H.A. Nguyen: conceptualization, methodology, formal analysis, writing-review & editing; writing-original draft; N. L. N. Trang: validation, investigation; M. K. Pham: validation, investigation; H. V. Tuan: methodology, investigation, supervision; A. T. Le: conceptualization, methodology, supervision, project administration, writing-review & editing.

Conflicts of interest

The authors declare that they have no known competing financial interests or personal relationships that could have appeared to influence the work reported in this paper.

Acknowledgements

References

1 A. Huefner, W. L. Kuan, K. H. Müller, J. N. Skepper, R. A. Barker and S. Mahajan, Characterization and visualization of vesicles in the endo-lysosomal pathway with surface-enhanced raman spectroscopy and chemometrics, *ACS Nano*, 2016, **10**(1), 307–316, DOI: 10.1021/acsnano.5b04456.

2 J. Su, *et al.*, Multicolor Gold-Silver Nano-Mushrooms as Ready-to-Use SERS Probes for Ultrasensitive and Multiplex DNA/miRNA Detection, *Anal. Chem.*, 2017, **89**(4), 2531–2538, DOI: 10.1021/acs.analchem.6b04729.

3 K. Sivashanmugan, J. Der Liao, B. H. Liu, C. K. Yao and S. C. Luo, Ag nanoclusters on ZnO nanodome array as hybrid SERS-active substrate for trace detection of malachite green, *Sens. Actuators, B*, 2015, **207**(Part A), 430–436, DOI: 10.1016/j.snb.2014.10.088.

4 J. Huang, D. Ma, F. Chen, M. Bai, K. Xu and Y. Zhao, Ag Nanoparticles Decorated Cactus-Like Ag Dendrites/Si Nanoneedles as Highly Efficient 3D Surface-Enhanced Raman Scattering Substrates toward Sensitive Sensing, *Anal. Chem.*, 2015, **87**(20), 10527–10534, DOI: 10.1021/acs.analchem.5b02788.

5 V. Kiran and S. Sampath, Enhanced raman spectroscopy of molecules adsorbed on carbon-doped TiO 2 obtained from titanium carbide: A visible-light-assisted renewable substrate, *ACS Appl. Mater. Interfaces*, 2012, **4**(8), 3818–3828, DOI: 10.1021/am300349k.

6 H. Zhang, S. Yang, Q. Zhou, L. Yang, P. Wang and Y. Fang, The Suitable Condition of Using LSPR Model in SERS: LSPR Effect Versus Chemical Effect on Microparticles Surface-Modified with Nanostructures, *Plasmonics*, 2017, **12**(1), 77–81, DOI: 10.1007/s11468-016-0231-4.

7 G. McNay, D. Eustace, W. E. Smith, K. Faulds and D. Graham, Surface-enhanced Raman scattering (SERS) and surface-enhanced resonance raman scattering (SERRS): A review of applications, *Appl. Spectrosc.*, 2011, **65**(8), 825–837, DOI: 10.1366/11-06365.

8 T. Tan, *et al.*, LSPR-dependent SERS performance of silver nanoplates with highly stable and broad tunable LSPRs prepared through an improved seed-mediated strategy, *Phys. Chem. Chem. Phys.*, 2013, **15**(48), 21034–21042, DOI: 10.1039/c3cp52236a.

9 L. Jensen, C. M. Aikens and G. C. Schatz, Electronic structure methods for studying surface-enhanced Raman scattering, *Chem. Soc. Rev.*, 2008, **37**(5), 1061–1073, DOI: 10.1039/b706023h.

10 A. Musumeci, *et al.*, SERS of semiconducting nanoparticles (TiO 2 hybrid composites), *J. Am. Chem. Soc.*, 2009, **131**(17), 6040–6041, DOI: 10.1021/ja808277u.

11 L. Zhou, *et al.*, Irreversible accumulated SERS behavior of the molecule-linked silver and silver-doped titanium dioxide hybrid system, *Nat. Commun.*, 2020, **11**(1), 1–10, DOI: 10.1038/s41467-020-15484-6.

12 L. Yang, X. Jiang, W. Ruan, B. Zhao, W. Xu and J. R. Lombardi, Observation of enhanced Raman scattering for molecules adsorbed on TiO 2 nanoparticles: charge-transfer contribution, *J. Phys. Chem. C*, 2008, **112**(50), 20095–20098, DOI: 10.1021/jp8074145.

13 D. T. N. Nga, *et al.*, A manganese dioxide–silver nanostructure-based SERS nanoplatform for ultrasensitive tricyclazole detection in rice samples: effects of semiconductor morphology on charge transfer efficiency and SERS analytical performance, *Phys. Chem. Chem. Phys.*, 2023, **25**, 17496–17507.

14 J. Zhou, *et al.*, Plasmon-induced hot electron transfer in Au-ZnO heterogeneous nanorods for enhanced SERS, *Nanoscale*, 2019, **11**(24), 11782–11788, DOI: 10.1039/c9nr02969a.

15 A. Peyravi, F. Ahmadijokani, M. Arjmand and Z. Hashisho, Graphene oxide enhances thermal stability and microwave absorption/regeneration of a porous polymer, *J. Hazard. Mater.*, 2022, **433**, 128792, DOI: 10.1016/j.jhazmat.2022.128792.

16 F. Khan, M. S. Khan, S. Kamal, M. Arshad, S. I. Ahmad and S. A. A. Nami, Recent advances in graphene oxide and reduced graphene oxide based nanocomposites for the photodegradation of dyes, *J. Mater. Chem. C*, 2020, **8**(45), 15940–15955, DOI: 10.1039/d0tc03684f.

17 M. Kim, M. Yoo, Y. Yoo and J. Kim, Capacitance behavior of composites for supercapacitor applications prepared with different durations of graphene/nanoneedle MnO2 reduction, *Microelectron. Reliab.*, 2014, **54**(3), 587–594, DOI: 10.1016/j.microrel.2013.11.005.

18 M. Zhang, *et al.*, The influences of graphene oxide (GO) and plasmonic Ag nanoparticles modification on the SERS sensing performance of TiO2 nanosheet arrays, *J. Alloys Compd.*, 2021, **864**, 158189, DOI: 10.1016/j.jallcom.2020.158189.

19 Y. Wang, *et al.*, Facile fabrication of Ag/graphene oxide/TiO2 nanorod array as a powerful substrate for photocatalytic degradation and surface-enhanced Raman scattering detection, *Appl. Catal., B*, 2019, **252**(April), 174–186, DOI: 10.1016/j.apcatb.2019.03.084.

20 D. T. Nguyet Nga, *et al.*, Elucidating the roles of oxygen functional groups and defect density of electrochemically exfoliated GO on the kinetic parameters towards furazolidone detection, *RSC Adv.*, 2022, **12**(43), 27855–27867, DOI: 10.1039/d2ra04147b.

21 M. Q. Doan, *et al.*, Ultrasensitive Detection of Methylene Blue Using an Electrochemically Synthesized SERS Sensor Based on Gold and Silver Nanoparticles: Roles of Composition and Purity on Sensing Performance and Reliability, *J. Electron. Mater.*, 2022, **51**(1), 150–162, DOI: 10.1007/s11664-021-09228-5.

22 D. T. Nguyet Nga, *et al.*, A manganese dioxide–silver nanostructure-based SERS nanoplatform for ultrasensitive tricyclazole detection in rice samples: effects of semiconductor morphology on charge transfer efficiency and SERS analytical performance, *Phys. Chem. Chem. Phys.*, 2023, **25**(26), 17496–17507, DOI: 10.1039/D3CP01592K.

23 G. Yan, *et al.*, Adsorption-Oxidation Mechanism of δ-MnO₂ to Remove Methylene Blue, *Adsorpt. Sci. Technol.*, 2021, **2021**, 3069392, DOI: **10.1155/2021/3069392**.

24 L. G. Cançado, M. A. Pimenta, B. R. A. Neves, M. S. S. Dantas and A. Jorio, Influence of the atomic structure on the Raman spectra of graphite edges, *Phys. Rev. Lett.*, 2004, **93**(24), 5–8, DOI: **10.1103/PhysRevLett.93.247401**.

25 Q. Q. Li, *et al.*, Rapid and sensitive detection of pesticides by surface-enhanced Raman spectroscopy technique based on glycidyl methacrylate-ethylene dimethacrylate (GMA-EDMA) porous material, *Chin. Chem. Lett.*, 2013, **24**(4), 332–334, DOI: **10.1016/j.cclet.2013.02.002**.

26 A. J. Kora and J. Arunachalam, Green fabrication of silver nanoparticles by gum tragacanth (astragalus gummifer): A dual functional reductant and stabilizer, *J. Nanomater.*, 2012, **2012**, 869765, DOI: **10.1155/2012/869765**.

27 X. Qiao, S. Liao, C. You and R. Chen, Phosphorus and Nitrogen Dual Doped and Simultaneously Reduced Graphene Oxide with High Surface Area as Efficient Metal-Free Electrocatalyst for Oxygen Reduction, *Catalysts*, 2015, **5**, 981–991, DOI: **10.3390/catal5020981**.

28 S. Zhang, W. Li, H. Tang, T. Huang and B. Xing, Revisit the adsorption of aromatic compounds on graphene oxide: Roles of oxidized debris, *Chem. Eng. J.*, 2022, **450**, 137996, DOI: **10.1016/j.cej.2022.137996**.

29 H. Tang, *et al.*, Wrinkle- and Edge-Adsorption of Aromatic Compounds on Graphene Oxide as Revealed by Atomic Force Microscopy, Molecular Dynamics Simulation, and Density Functional Theory, *Environ. Sci. Technol.*, 2018, **52**(14), 7689–7697, DOI: **10.1021/acs.est.8b00585**.

30 H. Tang, *et al.*, Theoretical insight into the adsorption of aromatic compounds on graphene oxide, *Environ. Sci.: Nano*, 2018, **5**(10), 2357–2367, DOI: **10.1039/c8en00384j**.

31 T. N. Pham, *et al.*, Roles of Phase Purity and Crystallinity on Chloramphenicol Sensing Performance of CuCo2O4/CuFe2O4-based Electrochemical Nanosensors, *J. Electrochem. Soc.*, 2021, **168**(2), 26506, DOI: **10.1149/1945-7111/abde80**.

32 T. N. Pham, X. N. Pham, H. Thi Nguyen, T. Pham, Q. H. Tran and A.-T. Le, Exploiting the Balance Between Conductivity and Adsorption Capacity/Redox Electrocatalytic Ability In MIL-Based Porous Crystalline Materials for the Electrochemical Response, *J. Electrochem. Soc.*, 2022, **169**(5), 56521, DOI: **10.1149/1945-7111/ac707b**.

33 S. K. Ponnaiah, P. Periakaruppan and B. Vellaichamy, New Electrochemical Sensor Based on a Silver-Doped Iron Oxide Nanocomposite Coupled with Polyaniline and Its Sensing Application for Picomolar-Level Detection of Uric Acid in Human Blood and Urine Samples, *J. Phys. Chem. B*, 2018, **122**(12), 3037–3046, DOI: **10.1021/acs.jpcb.7b11504**.

34 T. N. Pham, *et al.*, An insight of light-enhanced electrochemical kinetic behaviors and interfacial charge transfer of CuInS(2)/MoS(2)-based sensing nanoplatform for ultra-sensitive detection of chloramphenicol, *Anal. Chim. Acta*, 2023, **1270**, 341475, DOI: **10.1016/j.aca.2023.341475**.

35 R. L. McCreery, *Raman spectroscopy for chemical analysis*, John Wiley & Sons, 2005.

36 B. Liu, P. Zhou, X. Liu, X. Sun, H. Li and M. Lin, Detection of Pesticides in Fruits by Surface-Enhanced Raman Spectroscopy Coupled with Gold Nanostructures, *Food Bioprocess Technol.*, 2013, **6**(3), 710–718, DOI: **10.1007/s11947-011-0774-5**.

37 Y. Fan, K. Lai, B. A. Rasco and Y. Huang, Determination of carbaryl pesticide in Fuji apples using surface-enhanced Raman spectroscopy coupled with multivariate analysis, *Lwt*, 2015, **60**(1), 352–357, DOI: **10.1016/j.lwt.2014.08.011**.

38 C. S. Shende, F. Inscore, A. Gift, P. Maksymiuk and S. Farquharson, Analysis of pesticides on or in fruit by surface-enhanced Raman spectroscopy, *Nondestruct. Sens. Food Safety, Qual. Nat. Resour.*, 2004, **5587**, 170, DOI: **10.1117/12.569595**.

39 X. T. Wang, W. S. Shi, G. W. She, L. X. Mu and S. T. Lee, High-performance surface-enhanced Raman scattering sensors based on Ag nanoparticles-coated Si nanowire arrays for quantitative detection of pesticides, *Appl. Phys. Lett.*, 2010, **96**(5), 2008–2011, DOI: **10.1063/1.3300837**.

40 A. B. Nowicka, M. Czaplicka, A. A. Kowalska, T. Szymborski and A. Kamińska, Flexible PET/ITO/Ag SERS Platform for Label-Free Detection of Pesticides, *Biosensors*, 2019, **9**(3), 111, DOI: **10.3390/bios9030111**.

41 Z. Zhang, Q. Yu, H. Li, A. Mustapha and M. Lin, Standing Gold Nanorod Arrays as Reproducible SERS Substrates for Measurement of Pesticides in Apple Juice and Vegetables, *J. Food Sci.*, 2015, **80**(2), N450–N458, DOI: **10.1111/1750-3841.12759**.

42 L. L. Qu, Y. Y. Geng, Z. N. Bao, S. Riaz and H. Li, Silver nanoparticles on cotton swabs for improved surface-enhanced Raman scattering, and its application to the detection of carbaryl, *Microchim. Acta*, 2016, **183**(4), 1307–1313, DOI: **10.1007/s00604-016-1760-4**.

43 B. Hu, D. W. Sun, H. Pu and Q. Wei, Rapid nondestructive detection of mixed pesticides residues on fruit surface using SERS combined with self-modeling mixture analysis method, *Talanta*, 2020, **217**(March), 120998, DOI: **10.1016/j.talanta.2020.120998**.